Article

Directed self-assembly of sub-10 nm particles: Role of driving forces and template geometry in packing and ordering

Shafigh Mehraeen, Mohamed ASBAHI, FuKe Wang, Joel K.W. Yang, Jianshu Cao, and Mei Chee Tan

Langmuir, **Just Accepted Manuscript** • DOI: 10.1021/acs.langmuir.5b01696 • Publication Date (Web): 06 Jul 2015

Directed self-assembly of sub-10 nm particles: Role of driving forces and template geometry in packing and ordering

Shafigh Mehraeen[†,‡], *Mohamed Asbahi*[§], *Wang Fuke*[§], *Joel K. W. Yang*[†,§], *Jianshu Cao*[‡], *Mei Chee Tan*[*,†]

[†]Pillar of Engineering Product Development, Singapore University of Technology and Design, Singapore 138682
[‡]Department of Chemistry, Massachusetts Institute of Technology, Cambridge, Massachusetts 02139, United States
[§]Institute of Materials Research and Engineering, Agency for Science, Technology and Research (A*STAR), Singapore 117602

KEYWORDS: Directed self-assembly, templated self-assembly, template geometry, close packing, ordering.

ABSTRACT

By comparing the magnitude of forces, a directed self-assembly mechanism has been suggested[1] previously in which immersion capillary is the only driving force responsible for packing and ordering of nanoparticles, which occur only after the meniscus recedes. However, this mechanism is insufficient to explain vacancies formed by directed self-assembly at low particle concentrations. Utilizing experiments, and Monte Carlo and Brownian dynamics simulations, we developed a theoretical model based on a new proposed mechanism. In our proposed mechanism, the competing driving forces controlling the packing and ordering of sub-10 nm particles are (1) the repulsive component of the pair potential, and (2) the attractive capillary forces, both of which apply at the contact line. The repulsive force arises from the high particle concentration, and the attractive force is caused by the surface tension at the contact line. Our theoretical model also indicates that the major part of packing and ordering of nanoparticles occurs before the meniscus recedes. Furthermore, utilizing our model, we are able to predict the various self-assembly configurations of particles as their size increases. These results lay out the interplay between driving forces during directed self-assembly, motivating a better template design now that we know the importance and the dominating driving forces in each regime of particle size.

INTRODUCTION

Over the last two decades, there have been a great deal of interest in materials manufacturing using self-assembly process, on flat or patterned substrates with applications in biotechnology[2], photonics[3], plasmonics[4], shape selection[5, 6], printing[7], and coating[8].

Coffee ring effect[9, 10] formed by evaporative self-assembly has been a primary driver for researchers to apply self-assembly technique as a cost effective approach for achieving

nanostructures with well controlled spatial arrangement; thus enabling scalability with minimal material wastage. Despite its convenience, self-assembly might seem very complex because the interplay of several driving forces dictates the assembly and ordering of its constituents. To better exploit the advantages of this technique, one requires a control over the magnitude and time scale of these forces, especially as the constituent's size decreases. As such directed self-assembly (DSA)[11, 12] is introduced to offer some control over the self-assembly of building blocks, direct them to desired positions on a template, and trap them by the geometry of confinement[13] provided by the templates.

Despite the advances in the current imaging technologies to visualize what is happening at small length scales, we are still far from achieving a general theoretical understanding of the interplay of driving forces[1] involved in the DSA process, especially when particle size becomes as small as several nanometers in diameter[14, 15, 16]. These forces include (1) particle-particle forces (van der Waals and repulsive forces), (2) particle-template forces[5, 6] (electrostatic, and curvature driven[28,29] forces), and (3) particle-fluid forces (capillary[12,15,17, 18, 19, 20, 21, 22, 23], convective[24, 25], evaporative[26, 27, 28], and Brownian[14, 15] forces). All of these forces interact at the contact line in directed (templated) self-assembly.

By comparing the magnitude of forces, a mechanism was previously suggested[1] in which immersion capillary force is the only driving force responsible for DSA of nanoparticles (DSA-n). Immersion capillary force[17, 18, 19, 20, 21, 23] also known as the line tension is caused by the tensile forces at the surface of the fluid film whose thickness should be smaller than the particle diameter. In this mechanism, attraction between particles begins after the meniscus recedes. In contrast to this immersion capillary force view, there have been reported instances in which adsorption in interstices[29], and convective forces[30] (in DSA of bilayers), are the main driving forces in DSA-n.

Our recent experimental observations[16] also suggests another possible mechanism of DSA-n in which the repulsive part of particles pair potential as well as attractive capillary forces are playing the major role. In our proposed mechanism, an attractive capillary force is applied by the meniscus onto the first layer of particles at the free surface of the contact line where the particles concentration is normally high. This attractive capillary force drives the neighbouring particles in the next layer towards the substrate until the repulsive component limits further particle movement, leading to ordering. As such, the interaction of these two attractive and repulsive forces plays a significant role in packing and ordering of particles at the moving contact line when the meniscus recedes. Overall, results in this work indicate that our model model can be predictive in nanoparticle DSA configurations and a better template design now that we know the dominating and the importance of driving forces in each regime of particle size.

THEORY AND EXPERIMENT

Our model demonstrates the effects of above mentioned driving forces on the DSA-n. This model also enables us to effectively correlate the effect of processing parameters (such as contact angle, and substrate pulling speed, direction or angle) on packing and ordering of self-assembled structures; however, in immersion capillary model[1], there is not such a correlation.

In our model, particles are represented by spheres upon which various forces are applied. We focus on the main dominant forces at the contact line. Since particles concentration at the contact line is high, multiple layers of particles are submerged in the liquid film. As such, the liquid film thickness at the contact line is greater than the particle diameter, and thus our model does not consider the immersion capillary force, which was previously suggested[1] to be the force governing DSA-n mechanism in the immersion capillary model as shown in Figure 1A. According to the immersion capillary model, particles are pushed towards the substrate only at the contact line (Figure 1A, left panel). They are packed and ordered by the immersion capillary force, or line tension after the meniscus recedes (Figure 1A, right panel).

In contrast to the immersion capillary model, our model primarily focuses on driving forces which are present before meniscus recedes, as shown in Figure 1B. In our proposed mechanism, there is a zone at the front of the contact line where the particles are pushed towards the substrate. In our model, the compressive (attractive) capillary force applied on the surface of nanoparticles at the contact line generates compressive force field in the bulk. This force field dissipates through the particle layers, and its magnitude decreases from the meniscus to the bulk, as color coded in Figure 1B, respective to red (large magnitude) to blue (small magnitude).

<<< Figure 1 >>>

Sub-10 nm particles used in this study are stabilized by an oleylamine coating. We rule out the possibility of major contribution of particle-particle as well as particle-wall electrostatic repulsion because of dominating particle stabilization forces and application of non-polar solvent (hexane) used in this work. In order to compare simulation results with experimental data, we take into consideration the steric repulsion as one of the main driving forces.

We also take into account the capillary force applied by the meniscus onto the particles intersecting the meniscus. To find the capillary force, we integrate the surface tension acting on the contact line positioned at distance h from the center of the particle intersecting the free surface, as shown in Figure 2A. The magnitude of the resultant force can be written as

$$F_C = 2\pi\sigma\left(a - \frac{h^2}{a}\right)\cos\theta \quad (1)$$

whose horizontal and vertical components are $F_C \sin\psi$, and $f = F_C \cos\psi$, respectively. In Equation 1, σ is the surface tension, a is the particle radius, θ is the contact angle, and ψ is the meniscus angle with the substrate, as shown in Figure 2A.

<<< Figure 2 >>>

To consider major driving forces in DSA, we perform an order of magnitude analysis as follows. Steric repulsion potential of two nanoparticles induced by adsorbed polymer is expressed by [31]

$$V_{rep}(d) = 100\, k_B T a\, \delta^3 / (\pi d\, s^3) \exp(-\pi d/\delta) \quad (2)$$

where $k_B T$ is the thermal energy, δ is the thickness of ligand shell, and s is the distance of the two neighboring ligands on the surface of the particle, as illustrated in Figure 2B. Assuming $a = 5$ nm with separation distance of $d = 1$ nm, absorbed polymer layer thickness of $\delta = 1$ nm,

and $s = 1$ nm, excluding the exponential factor, we find that $V_{rep} \sim 160 k_B T$. We also find the order of magnitude for steric repulsion potential between the particles and the channel walls given by Alexander-d Gennes model[32, 33, 34]

$$V_w(d) = 16\pi k_B T \delta a d \, [28(d/2\delta)^{-5/4} - (20/11)(d/2\delta)^{7/4} + 12] / (35 s^3). \quad (3)$$

Using above parameters (see Figure 2C) renders a magnitude of $V_w \sim 560 k_B T$. A similar analysis for Hamaker attractive potential $V_{vdw}(d) = Aa/12d$ accounting for van der Waals interaction, reveals that $V_{vdw}(d) \sim k_B T$, where a common value of Hamaker constant when particles are very close to each other is $A = 0.4 k_B T$ [35].

Compressive capillary energy can be calculated from Equation 1, expressed by

$$V_C \sim 2\pi \sigma a^2 \cos\theta \quad (4)$$

Considering the reported hexane contact angle of $\theta = 40^o$ [36] with gold nanoparticles, and surface tension of $\sigma = 19$ pN/nm, we estimate the compressive capillary energy to be $\sim 560 k_B T$.

Immersion capillary energy is given by

$$V_{imm}(d) \sim 2\pi \sigma a^2 K_0(q[d + 2a]) \quad (5)$$

where K_0 is the modified Bessel function of order zero, and q^{-1} is the characteristic capillary length. For hexane as the solvent ($q^{-1} = 2.7 \times 10^6$ nm), we find that $V_{imm} \sim 9000 k_B T$. However, considering those forces acting at the contact line only, we exclude immersion capillary force, which is only effective after meniscus recedes.

The ratio of Brownian to van der Waals forces (and so energies) is commonly given by $12 k_B T d^2 / A a^2$. For 100 nm particles separated by 5 nm at room temperature, this ratio is about 0.01, indicating that Brownian forces is negligible for 100 nm or larger particles. However, for a 10 nm particle, this ratio is of order 1, indicating the significance of contribution of Brownian forces to the dynamics of 10 nm particles.

Considering above order-of-magnitude analysis, we only take into account repulsion pair potential, repulsive wall, compressive capillary, attractive Hamaker (van der Waals), and Brownian forces in this study.

To understand the impact of particle-particle, particle-fluid, and particle-template interactions on the final configuration of assemblages, we utilize our model to perform Monte Carlo (MC) simulations. Additionally, to gain insight into the dynamics of self-assembly, we perform Brownian dynamics (BD) simulations. We briefly explain these simulations below.

Monte Carlo simulation

MC simulation enables us to predict the steady state and kinetically trapped equilibrium configurations of assembled nanoparticles within the template. Each MC simulation starts with spheres initially positioned between the template walls in two horizontal layers parallel to the template base. These spheres are randomly distributed within each layer. To accommodate

experimental conditions[16], we set the simulation box sizes the same as those in the template consisting of graded channels of varying width. We consider a simulation trapezoid equal to one of the lithographically-defined channels, with a total length of 2 μm.

We run each MC simulation with total of 2×10^8 iteration steps. This number of iterations sufficiently equilibrates the total energy of the system. The total energy for each particle consists of the work done by the attractive capillary force and the pair potential between the particle and all other particles.

For each MC simulation, we obtain the final configuration of self-assembled particles by looking at the bottom layer only, consisting of 280 to 320 particles. In each MC step, we randomly select a sphere. For each selected sphere, moves along x-, y-, and z-directions are attempted separately. Step size for all moves is set to $0.007a$. Step size is changed adaptively to maintain the acceptance ratio between 0.49 and 0.51. After each move, we calculate the total energy change. To accept or reject each attempt, we utilize Metropolis algorithm[37] in which acceptance ratio of each move is Boltzmann weighted.

We consider the total energy for each particle in the form of

$$\beta U(d) = \beta f z + \beta V(d). \quad (6)$$

where $\beta = (k_B T)^{-1}$, d is the interparticle surface-to-surface spacing, and f is vertical component of the capillary force obtained from Equation 1 as explained before. The first term in Equation 6 represents the work done by the capillary force acted on each particle. For simplicity, we assume that f is downward along z-direction and perpendicular to the bottom of template. Also assuming that the meniscus angle is small ($\psi = 12^{o\ 43}$), we neglect the horizontal part of the capillary force for sub-10 nm particles. Using the surface tension of hexane, for each gold nanoparticles (AuNP), we set $\beta f = 100\ nm^{-1}$. The second term in Equation 6 is

$$V(d) = V_{rep}(d) + V_w(d) - V_{vdw}(d), \quad (7)$$

where $V_{rep}(d)$ is the steric repulsion potential (Equation 2), $V_w(d)$ is the repulsion wall potential (Equation 3), and $V_{vdw}(d)$ is the Hamaker attractive potential[39]. We set $\beta\varepsilon$ in Hamaker potential to unity[38] for AuNPs coated with oleylamine shell, and the distance between nearest neighbour particles at equilibrium in repulsion pair potential to $d_e = 2nm$.

Brownian dynamics simulation

BD simulation enables us to gain insight into the dynamics and kinetics of self-assembly. In BD simulation, we perform 10^9 simulation time steps each of which equals 0.1 ps in real time. Taking several hours to run, our simulations can represent approximately 100 μs of real time. However, experimental observations are much longer than this time scale. Thus, we use our BD simulations to make qualitative predictions regarding the pathways of nanoparticles self-assembly. The initial distribution and the template geometries are the same as those discussed above in MC simulation Section; however, without loss of generality we reduce the simulation box length to half of what was used in MC simulation to reduce the cost of computations and be able to make predictions at longer real time.

In MC simulations, to account for wall repulsion, we reject particle movements out of the simulation box. Accordingly, in BD simulations, we consider a wall repulsion potential, which decays very rapidly away from the channel walls. In these simulations, attractive capillary forces are applied only to those spheres that cross the moving angled meniscus. We keep a very thin liquid film behind the meniscus illustrating the effect of liquid bridges and line tension.

Neglecting electrostatic interactions between particles, their weight, and buoyancy force, we employ the following overdamped Langevin equations of motion to predict the dynamics of self-assembly of particles,

$$\xi \frac{d\vec{r}_i(t)}{dt} = \vec{F}_i(t) + \vec{B}_i(t) \tag{8}$$

where $\xi = 6\pi\eta a$ is the drag coefficient, $\vec{B}_i(t)$ is the Brownian force, and $\vec{F}_i(t)$ includes pair potential, repulsive wall, and capillary forces. In BD simulations, capillary forces are applied only to those particles that intersect the free surface as explained above. The magnitude of Brownian force in Equation 6 is chosen to obey the fluctuation-dissipation theorem

$$\langle \vec{B}_i(t), \vec{B}_j(t) \rangle = 2k_B T \xi \delta(t - t') \delta_{ij} I \,, \tag{9}$$

where δ_{ij} is the Kronecker delta, and $\vec{B}_i(t)$ is the Brownian force whose magnitude is

$$\left|\vec{B}_i\right| = 6\sqrt{\frac{\pi \eta a k_B T}{\Delta t}}, \text{ for any particle } i \,, \tag{10}$$

and I is the identity matrix. We use 2nd order Runge-Kutta method to integrate Equation 8 during a chosen time step $\Delta t = 0.1$ μs. For large particles (micron size or larger), the driving forces are gravitational, pair potential, capillary, and buoyancy forces (Brownian force is negligible for large particles), which will be discussed in the next Section.

To verify our model hypotheses in these simulations, we used a dip-coating technique. In a series of experiments, we systematically changed particles bulk concentration, pulling speed, angle, and direction. We explain our observations in these experiments as follows.

RESULTS AND DISCUSSION

We found that a high initial bulk concentration (1.67×10^{13} cm^{-3}) of particles is required to achieve maximum coverage and long range ordering. This finding is confirmed by our experimental observation in which reducing particle concentration, increases vacancies within the packing from Figure 3A to 3B. At very low concentrations, we do not observe any self-assembled structures shown in Figure 3C. Accordingly, density of spheres in our simulations mimics the concentration of particles at the contact line. In our MC simulations, we decrease the particle concentration from 100% to 10% of the initial maximum particle density. Figure 3D, from top to bottom, illustrates the corresponding self-assembled structures obtained from these MC simulations. The theoretical particle density obtained from our MC simulation results suggests that the maximum concentration, possibly at the contact line, is $\approx 4.2 \times 10^{17}$ cm^{-3}. This concentration is almost 4 orders of magnitude larger than experimental measurements done without dilution (1.67×10^{13} cm^{-3}), further away from the contact line in the bulk (see Section S3 in SI for relation between bulk and average contact line density).

<<< Figure 3 >>>

MC simulations results, shown in Figure 3D, qualitatively indicate the same trend observed experimentally in Figs. 3A, 3B and 3C, respectively, suggesting that lowering the concentration at the contact line increases the vacancies of assemblages and disruption of ordering. Thus, to reduce gaps between self-assembled clusters, it is necessary to create high bulk concentration. In this case, it is reasonable to assume that low lying particles very near the substrate feel compressive forces exerted by high lying ones accumulated at the contact line. These compressive forces mainly originate from the surface tension exerted onto the first layer of particles at the free surface. Low lying particles then feel these forces via pair potential interactions with first layer particles. The presence of such compressive force field between free surface and the substrate was indeed one of the assumptions of our model, as schematically shown in Figure 1B.

<<< Figure 4 >>>

We also observed that at a fixed concentration, increasing the pulling speed from low (0.1 mm/min, Figure 4A) to intermediate value (0.3 mm/min, Figure 4B), does not change the overall packing of self-assembled structure; however, by creating a convective flow and reducing the local concentration of particles at the contact line via applying a high pulling speed (1 mm/min, Figure 4C), many void regions were generated within clusters of particles. Taking a semi-quantitative approach, we observe that if vacancies appear (by increasing pulling speed) within the contact line before meniscus recedes, they will persist to exist after meniscus recedes. Unlike what was previously reported[1], our model implies that most ordering occurs before the meniscus recedes (see Figure 1B), and that the pressing component of capillary force is a critical factor in ordering. If immersion capillary forces alone were responsible for the ordering, then we would expect to see more chain-like structures[40], as opposed to patchy clusters, at low particle concentrations. Therefore, we propose that the major part of self-assembly ordering (which can sometimes be observed within several stacked layers of nanoparticles) is happening before the meniscus recedes.

Furthermore, our experimental results illustrated in Figure 4D, 4E, and 4F conducted at three different pulling angles (0, 45, 90 degrees, respectively), indicate that under a high initial bulk concentration (1.67×10^{13} cm^{-3}), self-assembly coverage and ordering is almost insensitive to the substrate pulling angle. This observation implies that hexane perfectly wets the substrate; therefore meniscus angle between substrate and meniscus is small and fixed regardless of pulling angle. Hence, the pressing capillary force at the free surface is always present and its magnitude is fixed. This conclusion is consistent with our hypothesis that ordering necessitates a permanent pressing capillary force with a fixed orientation with respect to the substrate. Furthermore, these experimental results demonstrate that the packing fraction is almost independent of pulling angle (from 0 to 90 degrees), which suggests that meniscus is tapered toward the contact line, making perpendicular (to the substrate) component of capillary force much larger than the parallel component. Having a perpendicular component much larger than the parallel component of capillary force was indeed another assumption of our model.

Our previous experimental results[16] show that surface coverage and ordering in the DSA with sub-10 nm particles does not change with the direction of meniscus motion. From these results, it is implied that in sub-10 nm particle DSA, the component of capillary force parallel to the substrate should be small; otherwise particles arrangement would be affected in the direction meniscus recedes. This finding is also consistent with our reported data[16] that pulling direction does not affect self-assembly coverage.

<<< Figure 5 >>>

Using our model, we now predict how geometry of template can impact the packing fraction and order-disorder transition. Figure 5 shows five MC simulations of order-disorder transitions along 2 μm long channels using the sphere model. In these simulations, the left-end channel width is kept fixed to 12 nm, while the right-end channel width increases from 34 to 74 nm, from top to bottom, respectively. The left and right end widths are shown along the y-axis on the left and right side in Figure 5, respectively. Obviously, packing fraction oscillates along the channel as one goes through successive ordered and disordered zones. It is insightful to look at how the packing fraction varies along the graded channel.

<<< Figure 6 >>>

Assuming that in the ordered zones, the average pitch stays constant[41] at p, one can predict the position of packing fraction maxima along the channel, which are connected by the blue lines as right-end channel width varies. The analytical form of the these blue lines, representing the distance of packing fraction maxima from the left end of the channel, x, is expressed by

$$x = \frac{L\left[\sigma + \frac{\sqrt{3}}{2}(n-1)p - D_1\right]}{(D_2 - D_1)}. \qquad (11)$$

where L is the channel length, D_1 and D_2 are the left- and right-end channel widths, respectively, and n is the number of rows of particles in the ordered zone. Equation 11 is shown by blue lines in Figure 5 for n=2, 3, 4, 5, and 6 rows of particles (marked by R_2 to R_6, respectively).

Using Equation 1`, one can also predict the separation between any two successive packing fraction maxima, which is the horizontal distance between blue lines, given by

$$\Delta x_{n\to(n+1)} = \frac{\sqrt{3}}{2}\frac{L\,p}{(D_2 - D_1)}. \qquad (12)$$

where $n \to (n+1)$ indicates the transition from n to $n+1$ rows of spheres. These results suggest that regardless of the channel gradient, ordered zones are formed and confined to the region where the channel width is commensurate with the particles pitch dictated by the repulsion-attraction pair potential. Particularly, parameter x has implications on how we can scale DSA process. It predicts that as long as we scale particle size (or the pitch, assuming the pitch is proportional to particle size), we can easily control the position of order-disorder transition zones by appropriately designing channel width, D.

We now look at the variation of packing fraction along the channel plotted against non-dimensionalized channel width, D/p, as illustrated in Figure 6, where $p = 12$ nm is the average pitch for 10 nm gold particles[16]. Coloring in Figure 6 indicates various channel gradients, from 0.011, 0.016, 0.021, 0.026 to 0.031, corresponding to red, blue, magenta, green, and black, respectively. The fact that all curves coincide indicates that order-disorder transitions occur at specific channel widths, i.e. packing fraction is independent of the channel gradient. Our MC simulation results also suggest that as channel width increases, the length of ordered zones decreases (as shown in Figure 5); thus maintaining high packing fraction become more difficult. This reduction in the length of ordered zone can also be seen from Figure 6 where the maximum packing fraction reduces as channel width increases. This reduction is also accompanied by an increase in packing fraction minimum. As we reach to ordered zones with 6 rows of particles (along the blue line marked by R_6 in Figures 5 and 6), the order-disorder transition zone widens. Configuration of particles at the peak of packing fraction in Figure 6 for different number of rows of particles (from 2 to 6) can be seen in Figure 5 along the blue lines marked by R_2 to R_6, respectively. Coloring in Figure 6, from red, blue, magenta, green, to black corresponds to packing fraction along channels shown in Figure 5 from top to bottom, respectively.

Furthermore, in Figure 6 we observe that there exists a threshold, D_s/p, and a plateau, ϕ_s, at which packing fraction eventually stabilizes to $\phi_s \sim 0.53$. Channel width larger than D_s resembles the bulk as if there is no channel wall. This indeed indicates the directed self-assembly on a flat substrate, whose packing fraction is marked by ϕ_s. This observation is in contrast to the compressed system[42], where the presence of external compressive force always increases the packing fraction. Results shown in Figure 6 consistently suggest that channel-width gradient does not affect packing fraction; it only controls the length of ordered and disordered zones. The coincidence of packing fraction for different channel gradient has also an implication that DSA of sub-10 nm particles in graded channels can be easily scaled using dimensionless parameter, D/p.

Comparing our previous MC simulation results[16] as well as those shown in Figure 6 with experimental data[16], we propose that the majority of packing and self-assembly configuration of particles is in fact formed before the meniscus recedes. We attribute such ordering and packing mostly to the coupled contribution from particle-particle repulsion and capillary force attraction pressing the particles downward. In the mechanism we propose here, the strong particle-particle and particle-wall attractive immersion capillary forces are indeed necessary to hold the particles in place after meniscus recedes. Our simulations results indicate that the absence of immersion capillary forces would result in disruption of previously formed ordered zones at the contact line after meniscus recedes. In our MC simulations, we found that repulsive component of pair potential is necessary to avoid particles penetration into one another. Furthermore, if the downward capillary force (see Equation 1) is removed from our model, we will not observe any of previously reported self-assembled structures[16] in the graded channels, suggesting the following overall self-assembly mechanism.

Particles are brought to the contact line by particle-fluid interactions, mainly by the convective flow, generated by the evaporation at the contact line as well as pulling of the substrate (flow of

liquid close to the substrate). Capillary forces applied by the moving contact line attract the particles at the contact line towards the substrate. From previous experimental data[7, 11] we estimate the contact line to be several hundreds of nanometres wide for 10 nm particles by assuming the width of contact line is proportional to the particle size, which is also consistent with our analytical calculations (see Section 2 in Supporting Information for details). This attractive force further increases the concentration of particles within the low lying layers of particles at the contact line, bringing the particles mostly into the repulsive regime of the pair potential. Interaction of this attractive capillary force with repulsive forces orders the packed assemblages of the particles at the contact line. Now meniscus recedes, contact line moves forward, and packed particles are left behind with a very thin film of liquid, creating immersion capillary forces. These immersion forces now help retain the particle arrangements until evaporation is completed.

The DSA mechanism explained above is also consistent with the dynamics of DSA captured by BD simulations of our model. Figure 7A illustrates five snapshots of the BD simulation of 90 particles of 10 nm in diameter, residing in a 500 nm long graded channel with left- and right-end channel dimensions of 14 and 31 nm, respectively. In Figure 7A, inclined blue surface represents the meniscus moving constantly from left to right with the angle of 12^{o} [43]. We distinguish between the spheres being in the top layers (white) or bottom layer (red). Increase of concentration in front of the moving meniscus is clear in Figure 7A (from top to bottom panel), where white spheres are accumulated in front of the meniscus. This accumulation gives rise to increase in the pair repulsion. If the concentration of spheres reaches to a level which cannot be completely pressed further from top to the bottom layer, spheres will be left in the top layers as meniscus recedes. Such excess concentration can be seen in the right end of the bottom panel in Figure 7A.

<<< Figure 7 >>>

Figure 7B illustrates the top view of the bottom layer, corresponding to the panels in Figure 7A (see Section 4 in Supporting Information for complete top view snapshots). It is remarkable to see how previously reported experimentally obtained open structures[16] are formed following the receding meniscus shown in Figure 7B. Specifically, the presence of the top layer helps form the hexagonal arrangement in the bottom layer of the ordered zone as soon as meniscus reaches to the part of channel in commensuration with the particles pitch.

To better understand the origin of above mentioned open structures, which one might attribute to the particle size effect, we compare BD simulations of 10 nm with those of 1.5 μm particles. We use the same particle concentration as that in Figure 7A, and resize the simulation box according to the particles diameter ratio. As the particle size increases, the attractive capillary and Brownian force increases (see Equations 1 and 10). These equations indicate that attractive capillary force is proportional to the particle size, whereas Brownian force is proportional to the square root of the particle size. Therefore, attractive capillary force increases more rapidly than Brownian force with the particle size; thus, attractive capillary force will be the dominating force for large particle size. We will further discuss the particle-size effect later in this section.

Figure 7C shows five snapshots of BD simulations of self-assembly of 1.5 μm particles, from top to bottom, respectively. From the top view of the graded channel, we find that self-assembled configurations of micron size particles are more compact than those of nanoparticles. We attribute this finding to much larger compressive capillary force compared to Brownian force for 1.5 μm particles, as shown in Figure 8. As such, we observe more compact structures in Figure 7C than Figure 7B. Also, due to the presence of large horizontal component of capillary force in micron size particles, DSA causes the particles to move along the direction of meniscus motion. This is in contrast to sub-10 nm particles DSA where Brownian motion strongly counteracts with the horizontal component of capillary force, making the self-assembly insensitive to the meniscus receding direction.

These simulation results suggest that most open structures observed in DSA of sub-10 nm particles[16] will not be present in DSA of micron size particles, and that DSA of large particles is highly sensitive to the meniscus receding direction. Furthermore, our proposed mechanism would work at both small and large length scales because both attractive capillary force and repulsion pair potential are still present; however, self-assembly configurations may vary since the magnitude of forces is altered with particle size, and Brownian forces are more pronounced at smaller length scale. We now consider these details in the context of size effect in DSA.

Particle-size effect analysis

To better understand the particle-size effect, we compare the magnitude of existing forces. These forces include capillary, repulsion pair potential, repulsive wall, and Brownian forces. All these forces are included in the equations of motion in Equation 8.

Capillary force is given by Equation 1 with an upper bound

$$F_c \approx 2\pi\sigma a\cos\theta . \quad (13)$$

Repulsion pair potential force can be obtained from steric repulsion potential[44] given by Equation 2. The magnitude of this repulsive force (excluding the exponential factor) is bounded above by

$$F_r \approx 100 k_B T a \delta^2 (\delta/(d\pi)+1)/(d s^3) . \quad (14)$$

For the purpose of comparison, we set the spacing between the ligands s=1 nm, particles surface-to-surface distance $d = a$, and ligand length $\delta = 0.2a$ [44, 45].

To account for steric repulsion between the particles and the channel walls, we use Alexander-de Gennes model[32, 33, 34] given by

$$F_w = 16\pi k_B T \delta a[7(d/2\delta)^{-5/4} + 5(d/2\delta)^{7/4} - 12]/(35 s^3), \quad (15)$$

where parameters are explained above.

Using Equation 10, one finds the Brownian force defined by

$$F_b = 6\sqrt{\pi\eta a\, k_B T/\Delta t}, \quad (16)$$

where for hexane, dynamic viscosity η=297×10^{-12} pN.s/nm^2. In our simulations, we set the simulation time step Δt = 0.1 μs.

Figure 8 compares the magnitude of various forces, using Equations 13 to 16, as particle size increases from 1 nm to 10 μm. All forces increase with particles size; however, the rate of increase of Brownian forces with the particle size is the smallest. For 1 nm particles, one can see that the ratio of repulsive or capillary to Brownian forces is larger than 8; this ratio increases as particle size becomes larger. For micron size particles or larger, all forces are at least 1000 larger than the Brownian forces, indicating that for such particles, Brownian forces are not dominating; thus Brownian forces can be neglected. These results are consistent with experimental data, indicating that controllability of DSA of micron size particles is much higher than that of nanoparticles. We attribute this ease in controllability of micron sized particle positioning to the absence of pronounced Brownian forces inherent to the nanoparticles.

<<< Figure 8 >>>

Overall, as the particle size increases, the physics of DSA stays the same, yet the dominating forces and sensitivity of packing and ordering to the forces as represented and directed by the coefficients change.

Furthermore, it is noteworthy that the current literature[1, 46, 47, 48] suggests that immersion capillary force (line tension) is the only dominant force governing the packing and ordering in DSA-n, and so the packing and ordering only occurs in the thin film left behind the meniscus. However, the formation of possible bilayers[11, 12, 30] or multilayers[30] behind the meniscus cannot be explained by immersion capillary force only, because in these cases particles are totally immersed[30]. We also believe that, to date, the interplay between meniscus-induced capillary force and repulsive part of pair potential due to high concentration at the contact line is overlooked.

CONCLUSION

By means of computational modelling, we show that repulsion pair potential, repulsive wall, Brownian, and capillary forces exerted by the meniscus onto the particles are critical determinant of packing and ordering in DSA-n. Qualitative visual inspection of DSA-n in graded channels from our computational modelling demonstrates that the compressive nature of capillary force accompanied by high concentration of particles forms self-assemblages, which are also observed experimentally. Experimental observations via systematic change of bulk concentration, pulling speed, angle, and direction is consistent with our model hypotheses implying that (i) a compressive capillary force perpendicular to the substrate always exists, (ii) self-assembly is insensitive to the pulling angles and directions, and (iii) any factor (such as particle concentration and pulling speed) interfering with the high concentration at the contact line can tremendously affect the assembly packing and ordering as observed experimentally. Furthermore, our computational modelling results suggest that immersion capillary force is mainly required to maintain the self-assembled particles intact after meniscus recedes.

To date, DSA has mostly been a phenomenological study that requires many time-consuming experiments involving multiple variables which have different influences upon varying templates. In this regard, our model can be predictive in a better template design now that we know the dominating and the importance of driving forces in each regime of particle size. Reproducing packing fraction and assemblages configurations in DSA of sub-10 nm particles[16],

the model developed in this work can also make DSA, particularly for particles confinement or trapping at sub-10 nm scale, a predictive process. However, more work needs to be accomplished to account for more complex template geometries, and convective forces due to evaporation process after meniscus recedes.

AUTHOR INFORMATION

Corresponding Author
*E-mail: meichee.tan@sutd.edu.sg

ACKNOWLEDGEMENTS

The work made use of the SERC nano Fabrication, Processing and Characterization (SnFPC) facilities in the Institute of Materials Research and Engineering (IMRE) in Singapore. S. Mehraeen, J. Cao and M. C. Tan gratefully acknowledge the support from the MIT-SUTD Postdoctoral Fellows Program.

ASSOCIATED CONTENT

Supporting Information. Modeling details of concentration effect on self-assembly configurations, estimation of the width of high concentration zone along the contact line, and detailed snapshots of BD simulations of DSA of 10 nm particles. This material is available free of charge via the Internet at http://pubs.acs.org.

ABBREVIATIONS

DSA, directed self-assembly; DSA-n, DSA of nanoparticles; BD, Brownian Dynamics; MC, Monte Carlo; SnFPC, SERC nano Fabrication, Processing and Characterization.

REFERENCES

(1) Liddle, J. A.; Cui, Y.; Alivisatos, P. Lithographically directed self-assembly of nanostructures. *J. Vac. Sci. Technol. B* **2004,** *22* (6), 3409-3414.
(2) Wink, T.; vanZuilen, S. J.; Bult, A.; vanBennekom, W. P. Self-assembled monolayers for biosensors. *Analyst* **1997,** *122* (4), R43-R50.
(3) Norris, D. J.; Vlasov, Y. A. Chemical approaches to three-dimensional semiconductor photonic crystals. *Adv. Mater.* **2001,** *13* (6), 371-376.
(4) Fan, J. A.; Bao, K.; Sun, L.; Bao, J. M.; Manoharan, V. N.; Nordlander, P.; Capasso, F. Plasmonic Mode Engineering with Templated Self-Assembled Nanoclusters. *Nano Lett.* **2012,** *12* (10), 5318-5324.
(5) Zhou, Y.; Zhou, X. Z.; Park, D. J.; Torabi, K.; Brown, K. A.; Jones, M. R.; Zhang, C.; Schatz, G. C.; Mirkin, C. A. Shape-Selective Deposition and Assembly of Anisotropic Nanoparticles. *Nano Lett.* **2014,** *14* (4), 2157-2161.
(6) Zhou, X. Z.; Zhou, Y.; Ku, J. C.; Zhang, C.; Mirkin, C. A. Capillary Force-Driven, Large-Area Alignment of Multi-segmented Nanowires. *Acs Nano* **2014,** *8* (2), 1511-1516.
(7) Kraus, T.; Malaquin, L.; Schmid, H.; Riess, W.; Spencer, N. D.; Wolf, H. Nanoparticle printing with single-particle resolution. *Nat. Nanotechnol.* **2007,** *2* (9), 570-576.
(8) Sellinger, A.; Weiss, P. M.; Nguyen, A.; Lu, Y. F.; Assink, R. A.; Gong, W. L.; Brinker, C. J. Continuous self-assembly of organic-inorganic nanocomposite coatings that mimic nacre. *Nature* **1998,** *394* (6690), 256-260.
(9) Deegan, R. D.; Bakajin, O.; Dupont, T. F.; Huber, G.; Nagel, S. R.; Witten, T. A. Capillary flow as the cause of ring stains from dried liquid drops. *Nature* **1997,** *389* (6653), 827-829.
(10) Lin, Z. *Evaporative self-assembly of ordered complex structures*; World Scientific: Singapore ; Hackensack, NJ, 2012. p xiv, 380 p.
(11) Yin, Y. D.; Lu, Y.; Gates, B.; Xia, Y. N. Template-assisted self-assembly: A practical route to complex aggregates of monodispersed colloids with well-defined sizes, shapes, and structures. *J Am Chem Soc* **2001,** *123* (36), 8718-8729.
(12) Xia, Y. N.; Yin, Y. D.; Lu, Y.; McLellan, J. Template-assisted self-assembly of spherical colloids into complex and controllable structures. *Adv. Funct. Mater.* **2003,** *13* (12), 907-918.
(13) Li, F.; Josephson, D. P.; Stein, A. Colloidal Assembly: The Road from Particles to Colloidal Molecules and Crystals. *Angewandte Chemie-International Edition* **2011,** *50* (2), 360-388.
(14) Cui, Y.; Bjork, M. T.; Liddle, J. A.; Sonnichsen, C.; Boussert, B.; Alivisatos, A. P. Integration of colloidal nanocrystals into lithographically patterned devices. *Nano Lett.* **2004,** *4* (6), 1093-1098.
(15) Korgel, B. A.; Fitzmaurice, D. Condensation of ordered nanocrystal thin films. *Phys. Rev. Lett.* **1998,** *80* (16), 3531-3534.
(16) Asbahi, M.; Mehraeen, S.; Lim, K. T. P.; Wang, F. K.; Cao, J.; Tan, M. C.; Yang, J. K. W. Template-induced structure transition in sub-10 nm self-assembling nanoparticles. *Nano Lett.* **2014,** *14*, 2642-2646.
(17) Kralchevsky, P. A.; Denkov, N. D.; Paunov, V. N.; Velev, O. D.; Ivanov, I. B.; Yoshimura, H.; Nagayama, K. Formation of 2-Dimensional Colloid Crystals in Liquid-Films under the Action of Capillary Forces. *Journal of Physics-Condensed Matter* **1994,** *6*, A395-A402.
(18) Kralchevsky, P. A.; Nagayama, K. Capillary interactions between particles bound to interfaces, liquid films and biomembranes. *Adv. Colloid Interface Sci.* **2000,** *85* (2-3), 145-192.

(19) Kralchevsky, P. A.; Nagayama, K. Capillary Forces between Colloidal Particles. *Langmuir* **1994,** *10* (1), 23-36.
(20) Kralchevsky, P. A.; Paunov, V. N.; Ivanov, I. B.; Nagayama, K. Capillary Meniscus Interaction between Colloidal Particles Attached to a Liquid-Fluid Interface. *J. Colloid Interface Sci.* **1992,** *151* (1), 79-94.
(21) Kralchevsky, P. A.; Paunov, V. N.; Denkov, N. D.; Nagayama, K. Capillary Image Forces .1. Theory. *J. Colloid Interface Sci.* **1994,** *167* (1), 47-65.
(22) Velev, O. D.; Denkov, N. D.; Paunov, V. N.; Kralchevsky, P. A.; Nagayama, K. Capillary Image Forces .2. Experiment. *J. Colloid Interface Sci.* **1994,** *167* (1), 66-73.
(23) Kralchevsky, P. A.; Denkov, N. D. Capillary forces and structuring in layers of colloid particles. *Curr. Opin. Colloid Interface Sci.* **2001,** *6* (4), 383-401.
(24) Delapierre, F. D.; Viovy, J. L.; Malaquin, L. Directed Assembly of Particles through Convective Flows and Capillary Forces. *Nanoscale Liquid Interfaces: Wetting, Patterning, and Force Microscopy at the Molecular Scale* **2013**, 577-620.
(25) Malaquin, L.; Kraus, T.; Schmid, H.; Delamarche, E.; Wolf, H. Controlled particle placement through convective and capillary assembly. *Langmuir* **2007,** *23* (23), 11513-11521.
(26) Bigioni, T. P.; Lin, X. M.; Nguyen, T. T.; Corwin, E. I.; Witten, T. A.; Jaeger, H. M. Kinetically driven self assembly of highly ordered nanoparticle monolayers. *Nat. Mater.* **2006,** *5* (4), 265-270.
(27) Suematsu, N. J.; Ogawa, Y.; Yamamoto, Y.; Yamaguchi, T. Dewetting self-assembly of nanoparticles into hexagonal array of nanorings. *J. Colloid Interface Sci.* **2007,** *310* (2), 648-652.
(28) Ohara, P. C.; Gelbart, W. M. Interplay between hole instability and nanoparticle array formation in ultrathin liquid films. *Langmuir* **1998,** *14* (12), 3418-3424.
(29) Pontoni, D.; Alvine, K. J.; Checco, A.; Gang, O.; Ocko, B. M.; Pershan, P. S. Equilibrating Nanoparticle Monolayers Using Wetting Films. *Phys. Rev. Lett.* **2009,** *102* (1), 016101.
(30) Denkov, N. D.; Velev, O. D.; Kralchevsky, P. A.; Ivanov, I. B.; Yoshimura, H.; Nagayama, K. Mechanism of Formation of 2-Dimensional Crystals from Latex-Particles on Substrates. *Langmuir* **1992,** *8* (12), 3183-3190.
(31) Owen, R. J.; Crocker, J. C.; Verma, R.; Yodh, A. G. Measurement of long-range steric repulsions between microspheres due to an adsorbed polymer. *Phys. Rev. E* **2001,** *64* (1), 011401.
(32) Degennes, P. G. Polymers at an Interface - a Simplified View. *Adv. Colloid Interface Sci.* **1987,** *27* (3-4), 189-209.
(33) Kamiyama, Y.; Israelachvili, J. Effect of Ph and Salt on the Adsorption and Interactions of an Amphoteric Polyelectrolyte. *Macromolecules* **1992,** *25* (19), 5081-5088.
(34) Zappone, B.; Ruths, M.; Greene, G. W.; Jay, G. D.; Israelachvili, J. N. Adsorption, lubrication, and wear of lubricin on model surfaces: Polymer brush-like behavior of a glycoprotein. *Biophys. J.* **2007,** *92* (5), 1693-1708.
(35) McKetta, J. J.; Cunningham, W. A. *Encyclopedia of chemical processing and design*; M. Dekker: New York, 1976. p v. <1-69>.
(36) Tavana, H.; Simon, F.; Grundke, K.; Kwok, D. Y.; Hair, M. L.; Neumann, A. W. Interpretation of contact angle measurements on two different fluoropolymers for the determination of solid surface tension. *J. Colloid Interface Sci.* **2005,** *291* (2), 497-506.
(37) Allen, M. P.; Tildesley, D. J. *Computer simulation of liquids*; Clarendon Press, Oxford University Press: Oxford England, 1987. p xix, 385 p.

(38) Hiemenz, P. C. R., R. "Principles of colloid and surface chemistry". *New York, Marcel Dekke* **1997**.
(39) Hamaker, H. C. The London - Van Der Waals attraction between spherical particles. *Physica* **1937,** *4*, 1058-1072.
(40) Nishikawa, H.; Maenosono, S.; Yamaguchi, Y.; Okubo, T. Self-assembling process of colloidal particles into two-dimensional arrays induced by capillary immersion force: A simulation study with discrete element method. *J. Nanopart. Res.* **2003,** *5* (1-2), 103-110.
(41) Asbahi, M.; Lim, K. T. P.; Wang, F. K.; Duan, H. G.; Thiyagarajah, N.; Ng, V.; Yang, J. K. W. Directed Self-Assembly of Densely Packed Gold Nanoparticles. *Langmuir* **2012,** *28* (49), 16782-16787.
(42) Pieranski, P.; Finney, J. Hard-Disk System - Structures of a Close-Packed Thin-Layer. *Acta Crystallogr. A* **1979,** *35* (Jan), 194-196.
(43) Drummond, C. J.; Chan, D. Y. C. van der Waals interaction, surface free energies, and contact angles: Dispersive polymers and liquids. *Langmuir* **1997,** *13* (14), 3890-3895.
(44) Weddemann, A.; Ennen, I.; Regtmeier, A.; Albon, C.; Wolff, A.; Eckstadt, K.; Mill, N.; Peter, M. K. H.; Mattay, J.; Plattner, C.; Sewald, N.; Hutten, A. Review and outlook: from single nanoparticles to self-assembled monolayers and granular GMR sensors. *Beilstein J Nanotech* **2010,** *1*, 75-93.
(45) Morrison, I. D.; Ross, S. *Colloidal dispersions : suspensions, emulsions, and foams*; Wiley-Interscience: New York, 2002. p xxvii, 616 p.
(46) Pavan, M. J.; Shenhar, R. Two-dimensional nanoparticle organization using block copolymer thin films as templates. *J. Mater. Chem.* **2011,** *21* (7), 2028-2040.
(47) Fisslthaler, E.; Blumel, A.; Landfester, K.; Scherf, U.; List, E. J. W. Printing functional nanostructures: a novel route towards nanostructuring of organic electronic devices via soft embossing, inkjet printing and colloidal self assembly of semiconducting polymer nanospheres. *Soft Matter* **2008,** *4* (12), 2448-2453.
(48) Pavan, M. J.; Ploshnik, E.; Shenhar, R. Nanoparticle Assembly on Topographical Polymer Templates: Effects of Spin Rate, Nanoparticle Size, Ligand, and Concentration. *J. Phys. Chem. B* **2012,** *116* (47), 13922-13931.

TOC Graphic

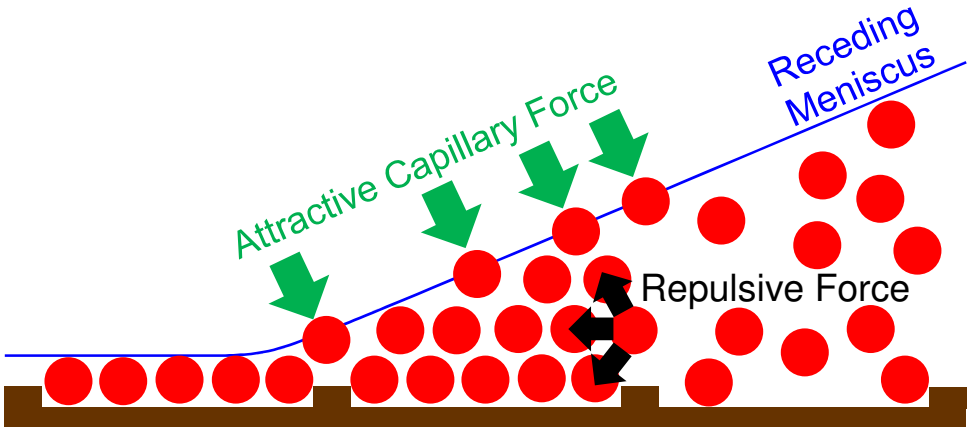

Packing and ordering in capillary assisted self-assembly can be achieved by interplay of attractive capillary and repulsive forces before meniscus recedes.

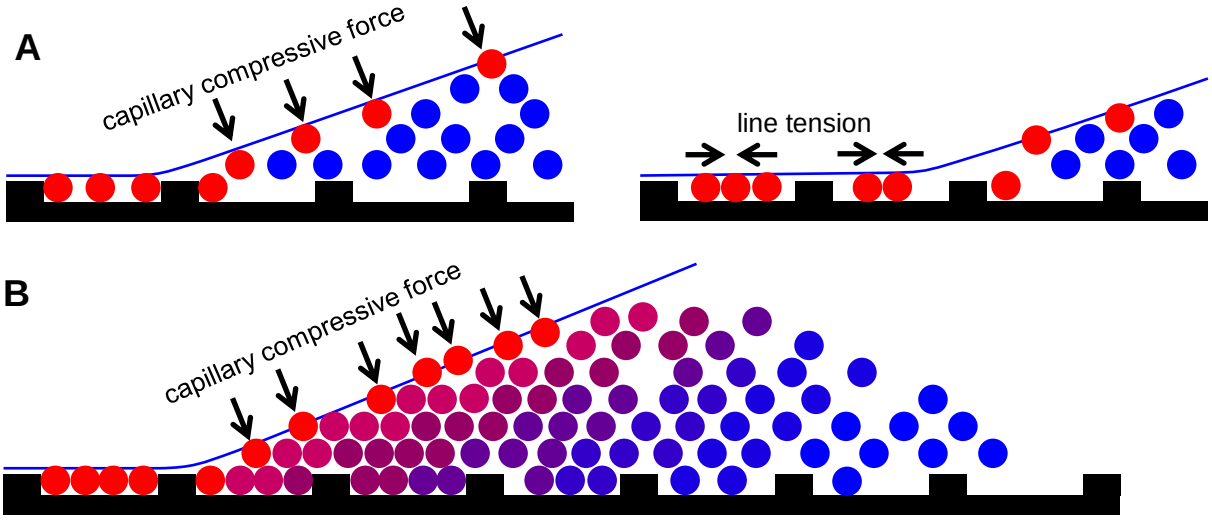

Figure 1. Panel A: Previously suggested mechanism of DSA-n by compressive capillary force (left panel) followed by the immersion capillary force or line tension after meniscus recedes (right panel). Panel B: Our proposed mechanism of DSA-n by a compressive force field generated by meniscus and particles pair potential, occurring when meniscus recedes. Coloring shows the strength of compressive force field (from red to blue respective to strong to weak).

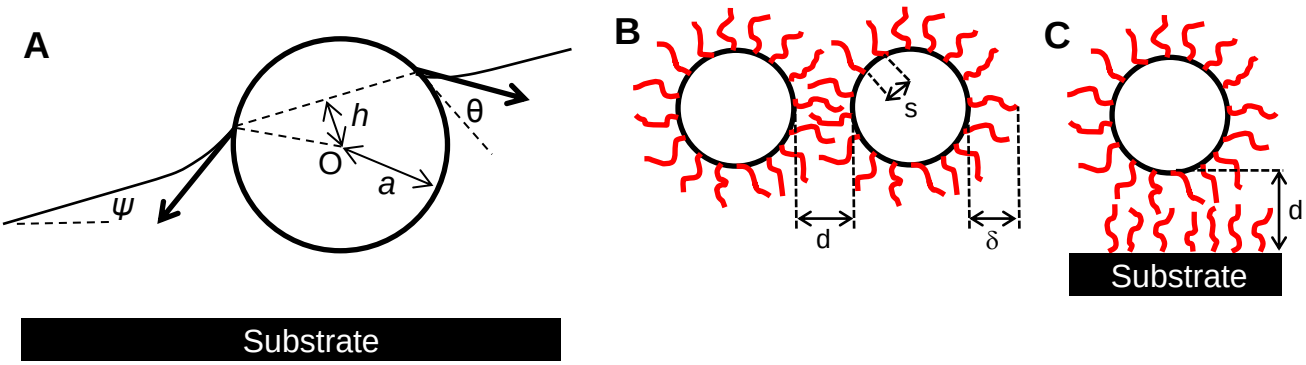

Figure 2. Panel A: Inclined meniscus applies a compressive capillary force onto the particle intersecting the free surface. The vertical component of this force presses the particle towards the substrate, while the horizontal component drags the particle along with the meniscus, moving from left to right. Panel B and C: Particles configurations and geometrical parameters used to evaluate repulsive forces during particle-particle, and particle-wall interactions, respectively.

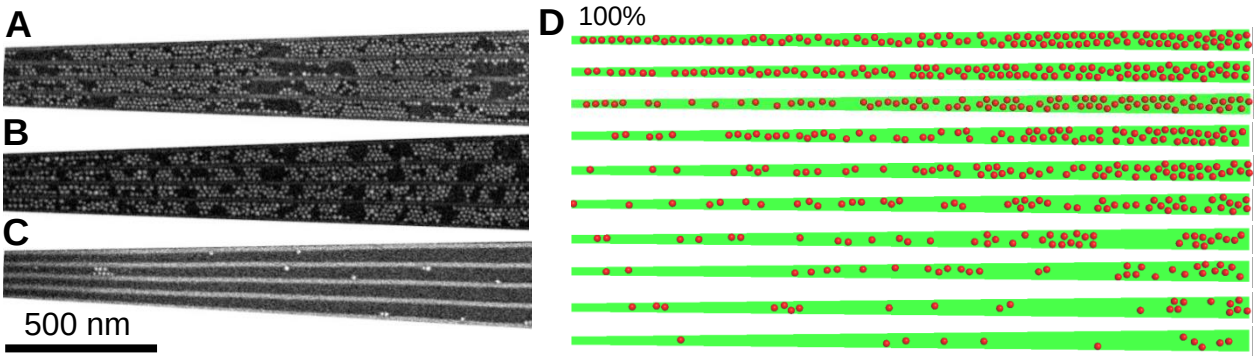

Figure 3. Fluid- and particle-particle interactions in the dip coating experiment. SEM images in panel A, B, and C illustrate the impact of particle concentration ($1.67, 0.28$, and $0.15\times10^{13}\,\mathrm{cm}^{-3}$, respectively) at constant pulling speed ($0.3\,\mathrm{mm/min}$). Panel D shows top view of 3D MC simulations, depicting the effect of contact line concentration of particles on the DSA-n configurations. Initial particle volume density decreases uniformly from top to bottom (from 100% to 10% of the maximum density of $4.2\times10^{17}\,\mathrm{cm}^{-3}$, respectively). Each simulation starts with particles randomly placed in the simulation box.

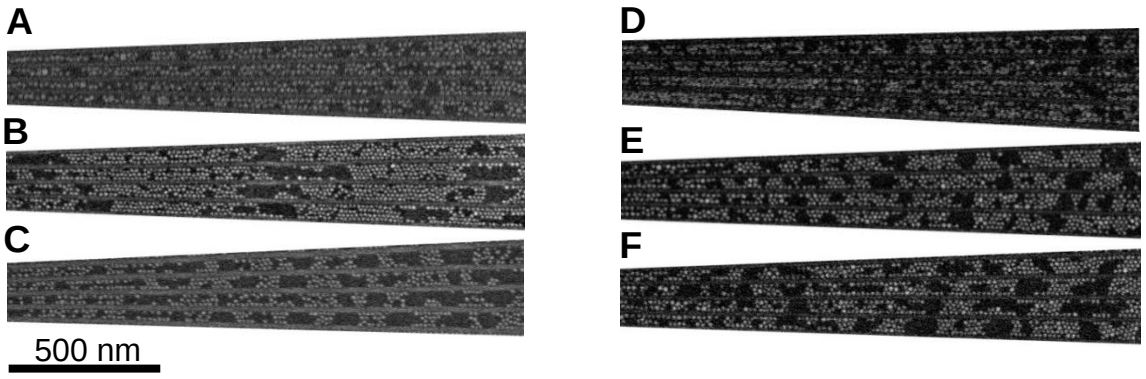

Figure 4. Template-particle interactions in the dip coating experiment. Panel A, B, and C illustrate that void regions increase with pulling speed ($0.1, 0.3$, and 1.0 mm/min, respectively) at constant particle concentration ($1.67\times10^{13}\mathrm{cm}^{-3}$). Panel D, E, and F show no effect on the DSA-n as pulling angle (0, 45, 90 degrees, respectively) increases at constant pulling speed (0.3 mm/min), and bulk concentration ($1.67\times10^{13}\mathrm{cm}^{-3}$).

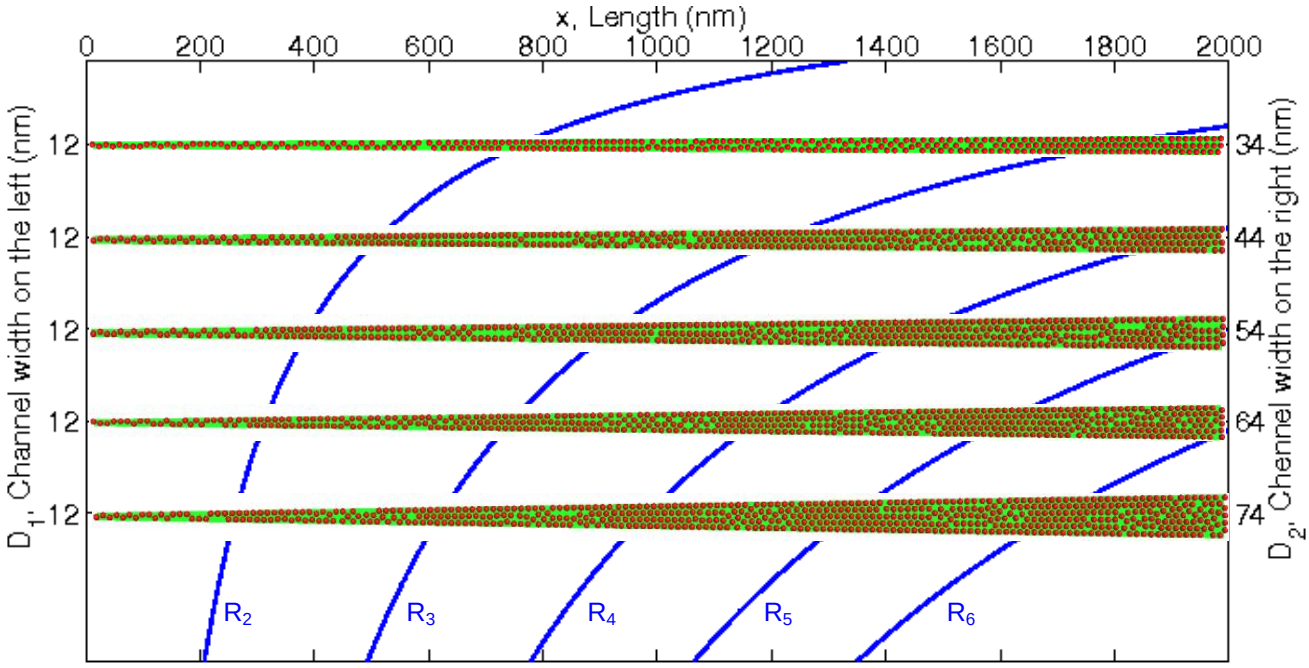

Figure 5. Prediction of position of packing fraction maxima (blue lines) vs distance along the channel, x. As channel gradient increases from top to bottom, the length of ordered zones, and the spacing between them decreases (see Equations 11 and 12 for details).

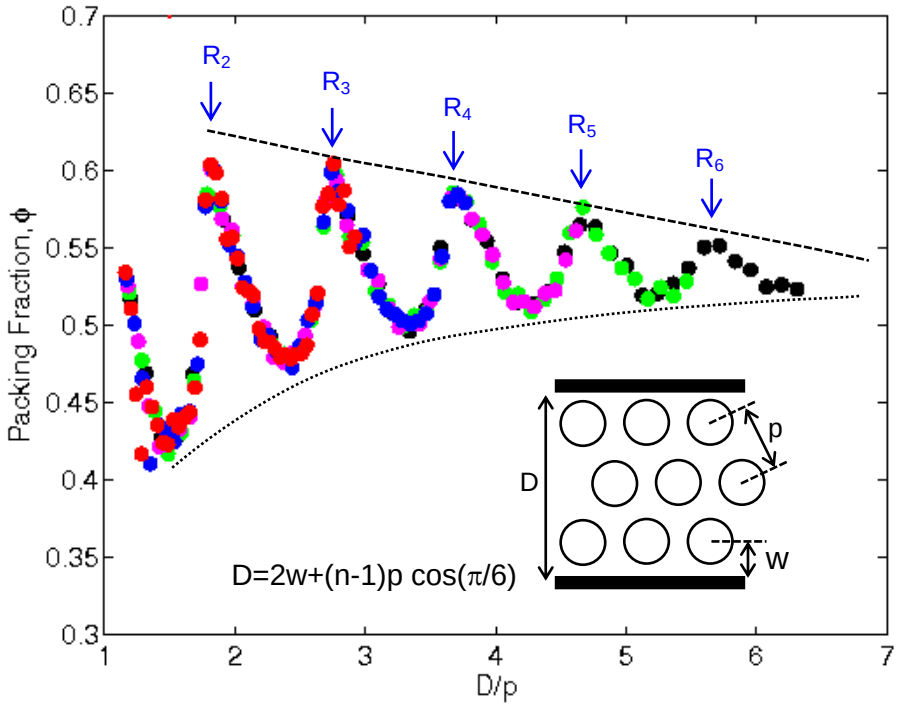

Figure 6. Maximum packing fraction (peaks) decreases as number of rows of particles in the self-assembled configuration increases from 2 to 6 (red, blue, magenta, green, to black, respective to the channels shown in Figure 5 from top to bottom). Packing fraction maxima and minima are independent of channel gradient. Dashed and dotted lines are guides for the eye, illustrating the decay of maxima and growth of minima of packing fraction. Inset shows the relation between channel width (D), wall distance (w), and particles pitch (p).

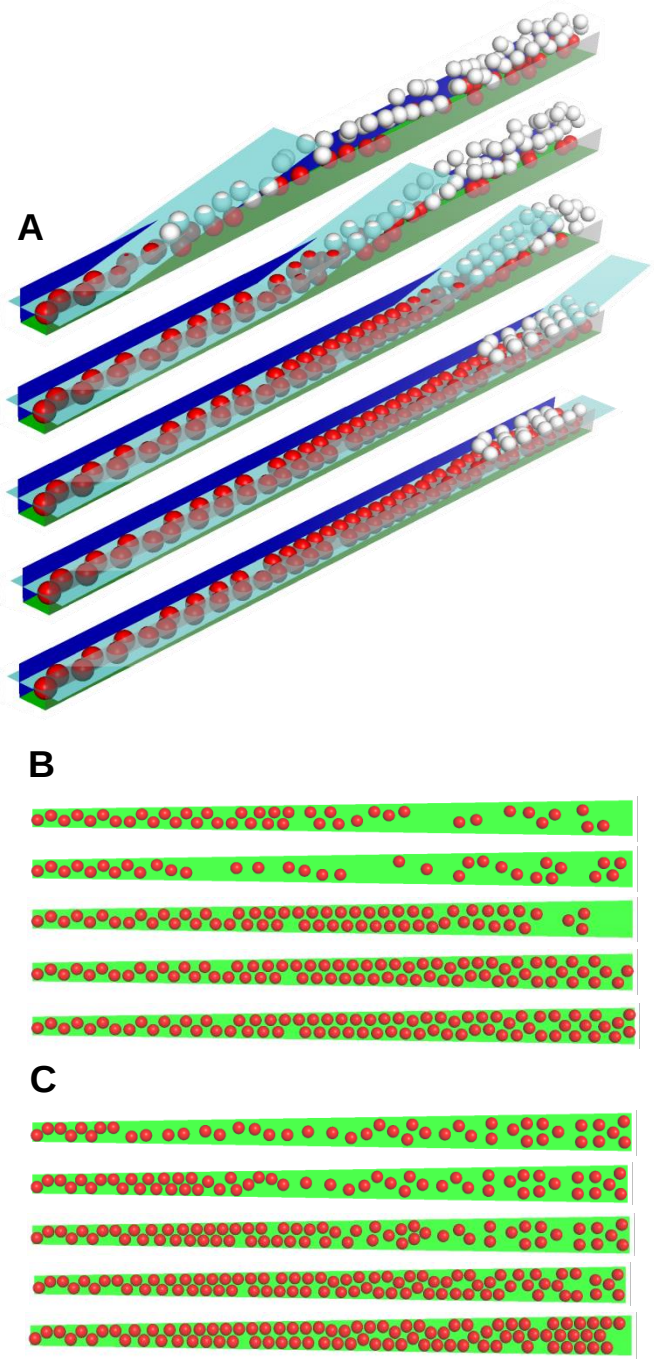

Figure 7. Panel A: BD simulation snapshots showing dynamics of self-assembly of 10 nm particles from top to bottom as the meniscus (transparent blue film) moves from left to right. Because of Brownian motion, disorder and vacancy defects can also be seen after meniscus recedes. Panel B: Top view of snapshots shown in panel A after the top layers of (white) particles are removed. Panel C: Top view of snapshots of BD simulation (resized to those in panel B) of self-assembly of 1.5 μm particles as meniscus recedes from left to right.

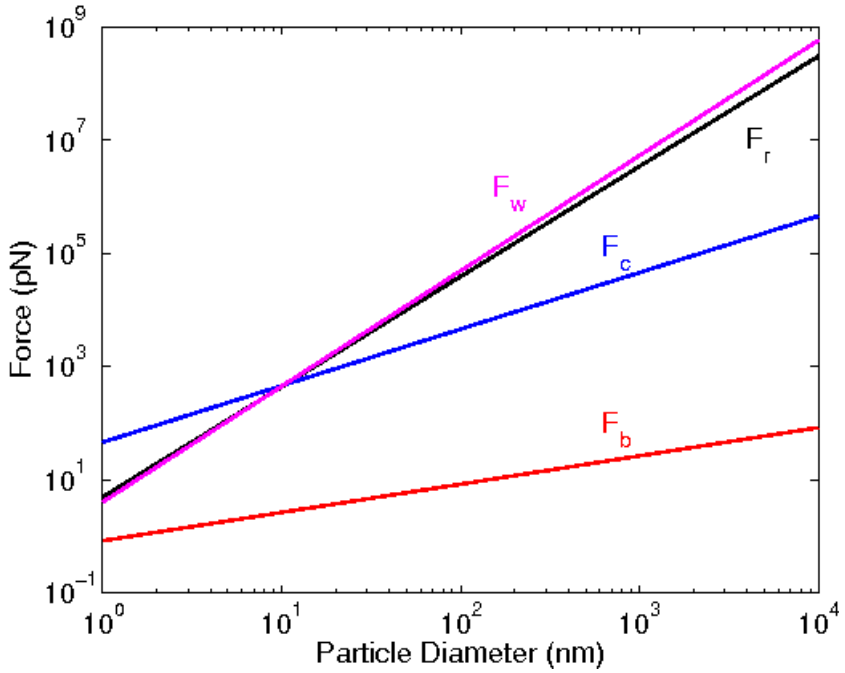

Figure 8. Comparison of wall (F_w, pink), repulsion pair-particle (F_r, black), capillary (F_c, blue), and Brownian (F_b, red) forces involved in DSA of particles against particles diameter. According to this figure, Brownian force becomes less important as particle size increases.